3D Printing of Solution-Processable 2D Nanoplates and 1D Nanorods for Flexible Thermoelectrics with Ultrahigh Power Factor at Low-Medium Temperatures

*Chaochao Dun, Wenzheng Kuang, Nicholas Kempf, Mortaza Saeidi-Javash, David J. Singh, and Yanliang Zhang**

Dr. C. Dun, W. Kuang, N. Kempf, M. Saeidi-Javash, Prof. Y. Zhang

Deapartment of Aerospace and Mechanical Engineering, University of Notre Dame, Notre Dame, Indiana 46556, USA

E-mail: yzhang45@nd.edu

Prof. D. J. Singh

Department of Physics and Astronomy, University of Missouri, Columbia, Missouri 65211, USA

Keywords: flexible thermoelectrics, 3D aerosol jet printing, 1D/2D nanocrystals

Abstract: Solution-processable semiconducting 2D nanoplates and 1D nanorods are attractive building blocks for diverse technologies, including thermoelectrics, optoelectronics, and electronics. However, transforming solution-processable colloidal nanopartricles into high-performance and flexible devices remains a challenge. For example, flexible films prepared by solution-processed semiconducting nanocrystals are typically plagued by poor thermoelectric and electrical transport properties. Here we report a highly scalable 3D conformal additive printing approach to directly convert solution-processed 2D nanoplates and 1D nanorods into high-performing flexible devices. The flexible films printed using Sb_2Te_3 nanoplates and subsequently sintered at 400 ^{0}C demonstrated exceptional thermoelectric power factor of 1.5 mW/m·K^2 over a wide temperature range (350-550 K). By synergistically combining Sb_2Te_3 2D nanoplates with Te 1D nanorods, the power factor of the flexible film reached an unprecedented maximum value of 2.2 mW/m·K^2 at 500 K, which is significantly higher than the best reported values for *p*-type flexible thermoelectric films. A fully printed flexible generator device exhibited a competitive electrical power density of 7.65 mW/cm^2 with a

reasonably small temperature difference of 60 K. The versatile printing method for directly transforming nanoscale building blocks into functional devices paves the way for developing not only flexible energy harvesters but also a broad range of flexible/wearable electronics and sensors.

1. Introduction

Flexible thermoelectric generators (*f*-TEGs) based on materials[1–6] such as Sb_2Te_3 and Bi_2Te_3,[7,8] carbon nanotube,[9] graphene,[10] conductive polymer and hybrids,[11] have the ability to interconvert thermal to electrical energy without moving parts. These *f*-TEGs can be integrated with portable/wearable electronics and sensors, and enable self-powered devices. In this context, V_2-VI_3 metal chalcogenides (Bi_2Te_3, Sb_2Te_3 and related alloys and compounds)[1,12–17] have attracted particular attention because of their high figure of merit (*ZT*) near room temperature.[18] For example, *p*-type Bi_2Te_3-Sb_2Te_3 alloys show high performance near room temperature and benefit considerably from nano-structuring.[19]

Similar to Bi_2Te_3, Sb_2Te_3 is also a topological insulator,[20] which leads to a complex, non-parabolic band structure, often highly favorable for thermoelectric (TE) performance.[21] It has an extremely high dielectric constant of ε_0~100, favorable for high mobility even with large concentration of defects.[22–24] Thus Sb_2Te_3 is potentially an important TE material, the key challenge being to find methods to control its carrier concentration and to effectively nanostructure the material while maintaining this control. So far, most of the reported Sb_2Te_3 related materials are *p*-type semiconductors. This is caused by intrinsic defects including Sb vacancies and anti-site defects of Sb atoms on the Te sites (Sb_{Te})[25] that occur during normal synthesis procedures. Typically, Sb_2Te_3 bulk single crystals stand out for their unique advantages including a high electrical conductivity (σ) around 3~5 $\times 10^5$ S/m, and a reasonable thermal conductivity (κ) around 1~6 W/m·K. However, Sb_2Te_3 also has a less competitive Seebeck coefficient (*S*) around 83~105 μV/K. This is due to its high degenerate hole

concentration (n>10^{20} cm^{-3}) created by the acceptor states mentioned above,[26] especially Sb_{Te}. Thus key problem is to find ways to control the doping level and thereby reduce the hole concentration and to determine the extent to which this can lead to enhanced *S* and TE performance. Nanostructuring has been employed to enhance *S*, and to reduce κ as a result of the increased phonon scattering effect.[19,27–30] For example, Sb_2Te_3 with 2D nanoplates morphology presents a 30% increase in *S* (*S*=125 μV/K) near room temperature.[31] *S* and *ZT* enhancement in nanostructured Sb_2Te_3 by anti-site defect suppression through sulfur doping was also achieved in nanobulk thermoelectrics.[32] Bi-Te and Sb-Te solid solutions (e.g. $Bi_{0.5}Sb_{1.5}Te_3$) also increase *S* (S>170 μV/K at 450 K) and suppress κ. Unfortunately, the reduced band gap limits the ability of the Bi-Sb-Te system to retain high ZT above 450 K.[33,34] Despite the high *ZT* (>1) observed in the Bi-Sb-Te system, the *ZT* normally peaks at narrow temperature range near or below 100 °C.[19,35–38] It has been an exacting challenge to develop materials with consistently high *ZT* with broad temperature plateau.[39,40] Meanwhile, there is also an absence of high *ZT* materials in the middle temperature range (200-300 °C) where the majority of the waste heat resides.[27]

Although TE nanostructures with enhanced *ZT* have been extensively studied, a big gap exists in translating these nanostructures into high-performance and flexible TE devices. The majority of reported TE devices were fabricated by exploiting the above mentioned inorganic nanostructures into bulk configurations.[41,42] However, rigid bulk devices not only consume large amount of TE materials but also present challenges in applications on curved surfaces such as the human body or even exhaust pipes.[15,43] We previously demonstrated an ultrafast photonic sintering method to process aerosol jet printed flexible $Bi_2Te_{2.7}Se_{0.3}$ *n*-type films. This led to a good room-temperature power factor (*PF*) of 0.73 $mWm^{-1}K^{-2}$.[17] While there have been recent advancements in flexible *n*-type films with competitive *PF*,[1,6] thermoelectrics need both *p*-type and *n*-type materials. The corresponding *PF* values for the flexible *p*-type films remain below or around 1 $mWm^{-1}K^{-2}$ (**Table S4**). In this work, a flexible *p*-type film with ultrahigh *PF* was fabricated based on a novel hybrid ink formulation consisting of 1D/2D nanostructures using a highly scalable 3D conformal aerosol jet printing method. The nanocomposite film printed using 2D Sb_2Te_3 nanoplates and 1D Te nanorods demonstrated a *PF* of 1.36 $mWm^{-1}K^{-}$

^{2} at room-temperature and a peak *PF* of 2.2 $mWm^{-1}K^{-2}$ at 500 K, which fills in a gap of the absence of high-performance and cost effective TE materials in the low-medium temperature range around 400-500 K.[47] In addition, we report theoretical work that elucidates the fundamental mechanisms leading to the enhanced power factor in this hybrid 2D/1D material. A fully printed flexible TE generator exhibits a high power density of 7.65 mW/cm^2 under a small temperature gradient of 60 K, demonstrating great potential to power wearable electronics and sensors.

2. Results and Discussion

Sb_2Te_3 nanoplates were fabricated using a facile energy-saving hydrothermal method (See details in the experimental section). **Figure 1(a-b)** shows the scanning electron microscopy (SEM) and high-resolution transmission electron microscopy (HRTEM) images of the 2D Sb_2Te_3 nanoplates with high crystallization. The lattice spacing of 0.209 nm corresponds to the lattice planes of (110) in Sb_2Te_3. **Figure S1** presents the powder X-ray diffraction (XRD) pattern of the as-fabricated Sb_2Te_3 plates, together with the major diffraction peaks which correspond to rhombohedral Sb_2Te_3 phase ($R\bar{3}m$, JCPDS No. 15-0874). No noticeable appearance of Te phase was observed. The average thickness of the plate is determined as 10 nm by the atomic force microscopy (AFM) analysis, with lateral size around 1~1.5 μm (**Figure S2)**. This highly anisotropic growth is derived from the inherent crystal structure of the material.[8] The as-fabricated Sb_2Te_3 nanoplates were cleaned by hydrazine hydrate and re-dispersed in a mixture of ethylene glycol (EG), glycerol and ethanol with optimized ratio of 35:5:60 wt%. The remaining polyvinylpyrrolidone (PVP) surfactant helps prevent the nanoplates from aggregation, which can be removed in the following sintering process.

Figure 1(c) describes the schematic of 3D conformal aerosol jet printing process using solution-processed nanostructures as building blocks, such as Sb_2Te_3 nanoplates. More printing details were provided in the experimental section and supporting information (SI) in **Table S1**. **Figure 1(d)** gives the optical image of the synthesized ink (concentration ~20 wt% of inorganic particles) with high stability that is printable for three months. Using the colloidal nanocrystal

ink, TE films with virtually any patterns can be produced by the present method onto both flat and curved substrates. The film thickness can be adjusted by controlling the ink concentration, the mass flow rate, and number of printing passes. For example, a dense and continuous Sb_2Te_3 thin film (thickness around 1.5 μm) was printed on polyimide (**Figure 1(e)**), with competitive internal resistance while maintaining excellent flexibility. **Figure 1(f)** shows the corresponding SEM image after sintering, revealing well connected Sb_2Te_3 networks that facilitate efficient charge carrier transport across neighboring nanoplates. Films printed on various substrates were obtained (**Figure 1(g-i)**), including patterns with different designs, and a thin-film printed on a cylindrical tube, demonstrating the promising ability of the present 3D conformal printing approach.

Thermal sintering plays an important role in removing the surfactant and consolidate the loose nanoparticle assembly into a densified continuous network. Here, a temperature of 400 ˚C is used in order to decompose and remove the remaining PVP surfactant. **Figure 2(a)** shows the temperature dependent electrical conductivity σ and Seebeck coefficient S measured along the in-plane direction of the sintered film. The film shows degenerate semiconducting behavior of decreasing σ with temperature, which is typical for Sb_2Te_3 nanostructures after sintering.[45] The σ is lower than that of the single-crystal bulk counterpart due to the electron scattering at the nano-grain boundaries. Nevertheless, the room-temperature σ reaches 7.8×10^4 S/m, which is among the highest reported values for printed TE films.[46,47] The carrier concentration (p) and mobility (μ) were determined by Hall measurement to be 1.01×10^{20} cm^{-3} and 48.5 $cm^2V^{-1}s^{-1}$, respectively. The high carrier concentration is in agreement with the Te-deficient defects as verified by energy-dispersive X-ray spectroscopy (EDS) analysis (**Figure S3** and **Table S2**), similar as previous study.[45] The Seebeck coefficient S also shows degenerate semiconductor behavior, i.e. S increases with increasing temperature. The room-temperature S of 130 μV/K, which is similar to that of the other Sb_2Te_3-based nanostructures,[31] is over 30% higher than

that of the single-crystal bulk counterpart.[26] The temperature dependent power factor (*PF*) is shown in **Figure 2(b)**, demonstrating a competitive value around 1.37 mW/m·K^2 at room temperature. It is noteworthy that the *PF* shows an average value of 1.5 mW/m·K^2 over a wide temperature plateau (350-550 K), which is promising for harvesting waste heat which is abundant in the low-to-middle temperature range. The flexibility of the film was also studied using repeated bending testing under different curvatures. A slight increase of 0.6% of the electrical resistance was observed over 1000 bending cycles with curvature radius around 7 mm, demonstrating excellent flexibility of the printed film.

To further increase the TE performance, a nanocomposite of mixed 2D Sb_2Te_3 plates and 1D Te nanorods was investigated, with fabrication details given in experimental section. When the atomic percent of Te precursor was over 60 at%, the crystalline Te was generated as an additional phase beyond Sb_2Te_3. XRD characterization of the nanocomposite was given in **Figure S4**. In this case, several Te peaks were observed beyond XRD pattern of Sb_2Te_3. About 8 wt % of excess tellurium was found in the form of tellurium nanorods based on EDS analysis and SEM characterization (**Figure S3** and **Table S2)**. Related temperature-dependent TE properties were presented in **Figure 3(a-b)**. The σ of the Sb_2Te_3-Te film decreases with the increasing temperature above 350 K, showing a metallic electron-phonon scattering dominated behavior similar to the above pure Sb_2Te_3 film. The nearly flat but slightly increasing σ with temperature below 350 K is likely due to the lower carrier concentration in the Sb_2Te_3-Te composite compared to that in the reference Sb_2Te_3, so that scattering processes (e.g. boundary scattering associated with the numerous interfaces) other than electron-phonon scattering become important in this temperature range. The room-temperature *S* shows a 13.1% increase from 130 to 147 μV/K, and the room-temperature *PF* maintains almost the same value as the pure Sb_2Te_3 film despite a small decrease of the σ with Te addition. The *S* of Sb_2Te_3-Te nanocomposite film keeps increasing to about 200 μV/K at 525 K (**Figure 3(a)**), which is about

16.3% higher than that of the Sb_2Te_3 film (~172 μV/K). Meanwhile, the σ of the Sb_2Te_3-Te film also surpasses that of the pure Sb_2Te_3 film when temperature exceeds 450 K. Comparison of the TE properties between Sb_2Te_3 and Sb_2Te_3-Te films is given in **Figure S5**. As a result, the *PF* of the Sb_2Te_3-Te film continues to increase monotonically and reaches a peak value of 2.2 mW/mK^2 at around 500 K, 46.7% higher than that of the Sb_2Te_3 film (**Figure 3(b)**). Comparison of TE performance of some representative *p*-type flexible films around room temperature was listed in **Table S4**. Our composite-based film can not only serve as power sources for flexible electronics around room temperature as the pure Sb_2Te_3 film, but also be used to recover waste heat in the low-medium temperature range around 400-500 K.[44]

TEM and high-resolution TEM images of printed Sb_2Te_3-Te film were given in **Figure 3(c-d)**. The Te precipitates are easily identified from the Sb_2Te_3 matrix from the lattice mismatch. As expected, the printed 1D/2D composite is composed of Sb_2Te_3 nanoplates and Te nanorods. The second phase Te appears as circular dots on the cross-section of the focused ion beam (FIB) milled film. The local EDS analysis and element line-scan (**Table S3** and **Figure S6**) confirmed the Te-rich phase of >85 at% Te. Here, the larger nanorods are formed during the sintering process, similar as previous reports.[34,48] The room temperature carrier concentration and mobility of the Sb_2Te_3–Te films were determined to be 4.95×10^{19} cm^{-3} and 79.3 $cm^2V^{-1}s^{-1}$, respectively.

Figure 4(a) shows the *S* obtained from Boltzmann transport calculations as a function of carrier concentration *p*. The *p* can be estimated by comparing experimental values with these curves. **Figure 4(b)** shows the calculated $S(T)$ for two carrier concentrations, specifically 4.3×10^{19} cm^{-3} and 6.1×10^{19} cm^{-3}. These values were chosen to be consistent with the ambient temperature experimental *S*. As can be seen, the curve for 4.3×10^{19} cm^{-3} is close to the experimental data of **Figure 3(a)** for Sb_2Te_3–Te system, while the higher doping level curve compares well with the Sb_2Te_3 data in **Figure 2(a)**. Note that the *p* in these theoretical curves is the chemical carrier

concentration, which is not the same as the Hall values due to the non-parabolic band structure. The similar temperature dependence of the calculated curves and the experimental data supports the inference that reduced doping level in the nanostructured Sb_2Te_3–Te leads to enhancement in *S*. The calculated electronic fitness function (EFF), shown in **Figure 4(c)**, measures the decoupling of *S* and σ through band structure effects, and is closely related to the *PF*. Importantly, Sb_2Te_3 has a complex band structure, strongly affected by spin-orbit coupling, related to its topological insulator nature. This deviates from a single parabolic band (SPB) model (**Figure S7**). The EFF shows both elevated values and an increase as carrier concentration is reduced from typical values of the bulk. This leads to high values in the carrier concentration range where *S* is consistent with the experimental values for nanostructured Sb_2Te_3-Te system.[49] The EFF indicates that the nanostructured Sb_2Te_3-Te is close to optimum doping at 500 K. It is also noteworthy that the calculated values of the EFF are quite high, reaching 1.3×10^{-19} $W^{5/3}m\ s^{-1/3}K^{-2}$ at 500 K. A value of 1.2×10^{-19} $W^{5/3}m\ s^{-1/3}K^{-2}$ is obtained at 300 K, albeit at lower carrier concentration. These values are comparable to some of the best TE materials.[49] The high EFF is connected with the topological insulator behavior of Sb_2Te_3, which leads to a highly non-parabolic band structure. This can be seen in the carrier pocket visualization of **Figure 4(d)**. Here, there are multiple, highly anisotropic carrier pockets, favorable for superior TE performance, and very different from the single spherical section characteristic of the isotropic parabolic band model.

Finally, a flexible/wearable TE generator with aerosol jet printed Sb_2Te_3-Te films and Ag electrodes was fabricated to demonstrate the printed *f*-TEG for energy harvesting, as can be seen in **Figure 5**. The output voltage and power show great promise for the development of small-scale flexible/wearable TE generators, where the high *PF* of the printed TE films plays a significant role. **Figure 5(a)** shows that the measured device open circuit voltage (V_{oc}) increases linearly with temperature difference (ΔT) by virtue of the Seebeck effect, achieving a maximum

output voltage of 36.6 mV at ΔT of 60 K with only 4 TE elements. **Figure 5(b-c)** shows the device operating voltage and power output as a function of electrical current tested at different ΔT, respectively. A maximum power output of 1.15 μW was obtained with a ΔT of 60 K when the external load resistance matches the internal resistance of the device. The device power density increases with ΔT and reaches 7.65 mW/cm^2 at ΔT of 60 K, as shown in **Figure 5(d)**. Here, the power density was evaluated based on the total cross-sectional area of the four TE elements perpendicular to the heat flow direction. The high power density indicates that a small size of the printed *f*-TEG is sufficient to power a range of typical internet of things and sensors.[50]

3. Conclusions

Creating functional materials with decent mechanical compliance while retaining competitive TE properties is a long-standing challenge. In this paper, high-performance and flexible thermoelectric films were produced by aerosol jet printing using solution-processable nanostructures. The power factor of printed Sb_2Te_3 films reaches 1.37 mW/mK^2 at around 300 K, with a competitive average power factor lager than 1.5 mW/mK^2 from 350 to 500 K. In addition, a 1D/2D nanocomposite film printed using a mixture of 1D Te nanorods and 2D Sb_2Te_3 nanoplates shows an ultrahigh peak power factor of 2.2 mW/mK^2 at 500 K, which is especially attractive for waste heat recovery applications at medium-temperature range. This is achieved by the control of carrier concentration near the optimum in the nanostructured composite film. A flexible all-printed thermoelectric generator was demonstrated, achieving a competitive device power density of 7.65 mW/cm^2 with a temperature difference of 60 K. The aerosol jet printing technique not only provides enormous opportunities in scalable manufacturing of flexible TE devices for energy harvesting and cooling application, but also can be readily applied to explore other device architectures for broad applications beyond thermoelectrics.

4. Experimental Section

*Nanoparticle fabrication***:** In a typical synthesis of pure Sb_2Te_3, 70 ml ethylene glycol (EG) solution containing mixed antimony trichloride ($SbCl_3$, 6 mmol), tellurium dioxide (TeO_2, 9 mmol), sodium hydroxide (NaOH, 1.5 g), and polyvinylpyrrolidone (PVP, $M_s \approx 40000$ g/mol, 0.8 g) were heated to 120 ˚C. 10 ml hydrazine hydrate (N_2H_4) was swiftly injected. The mixture was maintained at 130 ˚C for 30 minutes, then heated at 155 ˚C under reflux for another 10 hours. The precipitates were collected by centrifugation at 5000 rpm, washed using ethanol for another three times. To fabricate the Te-rich nanocomposite, a nominal 10 at% excess of TeO_2 was added with the other conditions remain the same. In the case when Te precursor is over 60 at%, additional Te is generated as a second phase.

Ink preparation and aerosol jet printing: The as-fabricated nanoplates were dispersed in solution to form a stable ink to allow aerosol jet printing (OPTOMEC AJP 300) using a pneumatic atomizer (PA). Normal inkjet printing has a strict requirement of viscosity of 5-15 cp. Aerosol jet printing, on the other hand, can print ink with viscosity from 1-1000 cp with different nanostructures, providing a versatile approach with high spatial resolution. The spatial resolution of the aerosol jet printing can reach approximately 20 μm in lateral dimension and several hundred nanometers in film thickness. In this work, the ink composition has been optimized to achieve optimal film deposition and all-printed TE devices. The solvent of Sb_2Te_3 ink is a mixture of ethylene glycol (EG), glycerol and ethanol with optimized composition of EG: Glycerol: Ethanol 35:5:60 wt%. After that, Sb_2Te_3 particles with weight ratio of 20% were added, followed by a strong probe sonication (20 minutes) and bath sonication (30 minutes).

Silver conductive ink (PRELECT TPS 50G2) was purchased from CLARIANT, and mixed with deionized water with volume ratio of 1:3 to prepare the Ag ink. Aerosol jet printer with ultrasonic atomizer (UA) is adopted to print Ag electrodes. All the printing parameters are summarized in the supporting information in **Table S1**.

Sintering of as-printed film: After cold press under 15 MPa for 15 minutes, thermal sintering was performed. The films were pre-heated at 110 ˚C for 1.5 hour to remove remaining solvent under N_2, and then sintered at 400 ˚C for 1 hour with an increasing rate of 1.5 ˚C/min, then decreased to 250 ˚C and hold for another 2 hours. Finally, the samples were cooled down to room temperature.

Characterizations: The synthesized Sb_2Te_3 nanoplates were analyzed by X-ray diffraction (XRD) using Cu Kα radiation (λ=1.5418 Å, Bruker D2 Phaser). Transmission Electron Microscope (TEM) and High Resolution TEM techniques including the selected area electron diffraction (SAED) images were performed using a JEM-2100 electron microscope. TEM specimens were prepared using focused ion beam (FIB) milling process, a FEI Helios FIB-SEM (FEI Company, Hillsboro, OR, USA) was used for serial sectioning and data collection. The morphology of all films (cross section and top-view) was measured by the Scanning Electron Microscope Magelllan 400 (FEI Company), with working voltage 15 KV and working distance 4.5 mm.

Thermoelectric properties measurement: Seebeck coefficient was measured with a transient method wherein the temperature difference is increased from 1 to 5 K at approximately 0.5 K/min. Electrical conductivity was measured before Seebeck coefficient when temperatures are held at steady state with less than 0.05 K/min change in absolute temperature and in temperature difference. More details about the measurement setup and method were given in **Figure S8**.

5. Computational Section

Transport and electronic structure calculations: Density functional calculations were performed for bulk Sb_2Te_3 with the Perdew-Burke-Ernzerhof Generalized Gradient Approximation (PBE-GGA).[51] The calculations were done using the general potential linearized augmented planewave method as implemented in the WIEN2k code.[52] Experimental lattice parameters were used, and the non-symmetry constrained atomic positions were

determined by total energy minimization. Transport calculations were done using the BoltzTraP code with the constant scattering time approximation.[53] The electronic fitness function was then obtained from the transport data using the transM code (http://faculty.missouri.edu/singhdj/transm.shtml).

Supporting Information

Supporting Information is available from the Wiley Online Library or from the author.

Acknowledgements

Chaochao Dun and Wenzheng Kuang contributed equally to this work. Y. Zhang acknowledges funding support from the National Science Foundation under award CMMI-1747685, DARPA under DARPA HR00111820030, and U.S. Department of Energy under award DE-NE0008712. Theoretical work performed at the University of Missouri was supported by the Department of Energy, Basic Energy Sciences, Award Number DE-SC0019114. We also would like to thank the Notre Dame Integrated Imaging Facility of University of Notre Dame to provide professional assist on material characterizations.

Received: ((will be filled in by the editorial staff))
Revised: ((will be filled in by the editorial staff))
Published online: ((will be filled in by the editorial staff))

References

[1] Q. Jin, S. Jiang, Y. Zhao, D. Wang, J. Qiu, D.-M. Tang, J. Tan, D.-M. Sun, P.-X. Hou, X.-Q. Chen, K. Tai, N. Gao, C. Liu, H.-M. Cheng, X. Jiang, *Nat. Mater.* **2019**, *18*, 62.

[2] Z. Lin, C. Hollar, J. S. Kang, A. Yin, Y. Wang, H. Y. Shiu, Y. Huang, Y. Hu, Y. Zhang, X. Duan, *Adv. Mater.* **2017**, *29*, 1606662.

[3] S. J. Kim, H. E. Lee, H. Choi, Y. Kim, J. H. We, J. S. Shin, K. J. Lee, B. J. Cho, *ACS Nano* **2016**, *10*, 10851.

[4] C. Wan, R. Tian, M. Kondou, R. Yang, P. Zong, K. Koumoto, *Nat. Commun.* **2017**, *8*, 1024.

[5] Y. Ding, Y. Qiu, K. Cai, Q. Yao, S. Chen, L. Chen, J. He, *Nat. Commun.* **2019**, *10*, 841.

[6] Y. Lu, Y. Qiu, K. Cai, Y. Ding, M. Wang, C. Jiang, Q. Yao, C. Huang, L. Chen, J. He, *Energy Environ. Sci.* **2019**, DOI 10.1039/c9ee01609k.

[7] T. Varghese, C. Hollar, J. Richardson, N. Kempf, C. Han, P. Gamarachchi, D. Estrada, R. J. Mehta, Y. Zhang, *Sci. Rep.* **2016**, *6*, 33135.

[8] C. Dun, C. A. Hewitt, Q. Li, Y. Guo, Q. Jiang, J. Xu, G. Marcus, D. C. Schall, D. L. Carroll, *Adv. Mater.* **2017**, *29*, 1702968.

[9] C. A. Hewitt, A. B. Kaiser, S. Roth, M. Craps, R. Czerw, D. L. Carroll, *Nano Lett.* **2012**, *12*, 1307.

[10] T. Juntunen, H. Jussila, M. Ruoho, S. Liu, G. Hu, T. Albrow-Owen, L. W. T. Ng, R. C. T. Howe, T. Hasan, Z. Sun, I. Tittonen, *Adv. Funct. Mater.* **2018**, *28*, 1800480.

[11] L. Wang, Z. Zhang, L. Geng, T. Yuan, Y. Liu, J. Guo, L. Fang, J. Qiu, S. Wang, *Energy Environ. Sci.* **2018**, *11*, 1307.

[12] Y. Zhang, T. Day, M. L. Snedaker, H. Wang, S. Krämer, C. S. Birkel, X. Ji, D. Liu, G. J. Snyder, G. D. Stucky, *Adv. Mater.* **2012**, *24*, 5065.

[13] J. S. Son, M. K. Choi, M. Han, K. Park, J. Kim, S. J. Lim, M. Oh, Y. Kuk, C. Park, S. Kim, T. Hyeon, *Nano Lett.* **2012**, *12*, 640.

[14] G. Zhang, B. Kirk, L. a Jauregui, H. Yang, X. Xu, Y. P. Chen, Y. Wu, *Nano Lett.* **2012**, *12*, 56.

[15] S. H. Park, S. Jo, B. Kwon, F. Kim, H. W. Ban, J. E. Lee, D. H. Gu, S. H. Lee, Y. Hwang, J. S. Kim, D. Bin Hyun, S. Lee, K. J. Choi, W. Jo, J. S. Son, *Nat. Commun.* **2016**, *7*, 1.

[16] G. Zhang, Q. Yu, W. Wang, X. Li, *Adv. Mater.* **2010**, *22*, 1959.

[17] M. Saeidi-javash, W. Kuang, C. Dun, Y. Zhang, *Adv. Fucntional Mater.* **2019**, 1901930.

[18] C. Dun, C. A. Hewitt, Q. Li, J. Xu, D. C. Schall, H. Lee, Q. Jiang, D. L. Carroll, *Adv. Mater.* **2017**, *29*, 1700070.

[19] B. Poudel, Q. Hao, Y. Ma, Y. Lan, A. Minnich, B. Yu, X. Yan, D. Wang, A. Muto, D. Vashaee, *Science (80-.).* **2008**, *320*, 634.

[20] H. Zhang, C.-X. Liu, X.-L. Qi, X. Dai, Z. Fang, S.-C. Zhang, *Nat. Phys.* **2009**, *5*, 438.

[21] H. Shi, D. Parker, M.-H. Du, D. J. Singh, *Phys. Rev. Appl.* **2015**, *3*, 014004.

[22] K. Ulutas, D. Deger, M. F. Kotkata, *J. Phys. Conf. Ser.* **2013**, *417*, 012040.

[23] X. He, D. J. Singh, P. Boon-on, M. Lee, L. Zhang, *J. Am. Chem. Soc.* **2018**, *140*, 18058.

[24] O. Madelung, U. Rössler, M. Schulz, Eds. , *Non-Tetrahedrally Bonded Elements and Binary Compounds 1*, Springer, Berlin, **1998**.

[25] Y. Jiang, Y. Y. Sun, M. Chen, Y. Wang, Z. Li, C. Song, K. He, L. Wang, X. Chen, Q. K. Xue, X. Ma, S. B. Zhang, *Phys. Rev. Lett.* **2012**, *108*, 1.

[26] H. Scherrer, S. Scherrer, in *CRC Press. London*, **1995**, p. 239.

[27] Y. Lan, A. J. Minnich, G. Chen, Z. Ren, *Adv. Funct. Mater.* **2010**, *20*, 357.

[28] H. Yang, J.-H. Bahk, T. Day, A. M. S. Mohammed, G. J. Snyder, A. Shakouri, Y. Wu, *Nano Lett.* **2015**, *15*, 1349.

[29] Y. Zhang, H. Wang, S. Kräemer, Y. Shi, F. Zhang, M. Snedaker, K. Ding, M. Moskovits, G. J. Snyder, G. D. Stucky, *ACS Nano* **2011**, *5*, 3158.

[30] S. Ortega, M. Ibáñez, Y. Liu, Y. Zhang, M. V. Kovalenko, D. Cadavid, A. Cabot, *Chem. Soc. Rev.* **2017**, *46*, 3510.

[31] W. Shi, L. Zhou, S. Song, J. Yang, H. Zhang, *Adv. Mater.* **2008**, *20*, 1892.

[32] R. J. Mehta, Y. Zhang, H. Zhu, D. S. Parker, M. Belley, D. J. Singh, *Nano Lett.* **2012**, *12*, 4523.

[33] M. Scheele, N. Oeschler, I. Veremchuk, K.-G. Reinsberg, A.-M. Kreuziger, A. Kornowski, J. Broekaert, C. Klinke, H. Weller, *ACS Nano* **2010**, *4*, 4283.

[34] Y. Liu, Y. Zhang, S. Ortega, Ibáñez, Maria, K. H. Lim, A. Grau-Carbonell, S. Martí-Sánchez, K. M. Ng, J. Arbiol, M. V. Kovalenko, D. Cadavid, A. Cabot, *Nano Lett.* **2018**, *18*, 2557.

[35] J. S. Son, H. Zhang, J. Jang, B. Poudel, A. Waring, L. Nally, D. V. Talapin, *Angew. Chemie* **2014**, *53*, 7466.

[36] G. Zheng, X. Su, H. Xie, Y. Shu, T. Liang, X. She, W. Liu, Y. Yan, Q. Zhang, C. Uher, M. G. Kanatzidis, X. Tang, *Energy Environ. Sci.* **2017**, *10*, 2638.

[37] Y. Ma, Q. Hao, B. Poudel, Y. Lan, B. Yu, D. Wang, G. Chen, Z. Ren, *Nano Lett.*

2008, *8*, 2580.

[38] G. Zheng, X. Su, X. Li, T. Liang, H. Xie, X. She, Y. Yan, C. Uher, M. G. Kanatzidis, X. Tang, *Adv. Energy Mater.* **2016**, *6*, 1600595.

[39] K. Peng, X. Lu, H. Zhan, S. Hui, X. Tang, G. Wang, *Energy Environ. Sci.* **2016**, *9*, 454.

[40] F. B. Te, P. Puneet, R. Podila, M. Karakaya, S. Zhu, J. He, T. M. Tritt, *Sci. Rep.* **2013**, *3212*, 1.

[41] X. Hu, P. Jood, M. Ohta, M. Kunii, K. Nagase, H. Nishiate, M. G. Kanatzidis, A. Yamamoto, *Energy Environ. Sci.* **2016**, *9*, 517.

[42] Y. Liu, G. García, S. Ortega, D. Cadavid, P. Palacios, J. Lu, M. Ibáñez, L. Xi, J. De Roo, A. M. Lopez, S. Martí, I. Cabezas, M. de la Mata, Z. Luo, C. Dun, O. Dobrozhan, D. Carroll, W. Zhang, J. C. Martins, M. Kovalenko, J. Arbiol, G. Noriega, J. Song, P. Wahnon, A. Cabot, *J. Mater. Chem. A* **2017**, *5*, 2592.

[43] F. Kim, B. Kwon, Y. Eom, J. E. Lee, S. Park, S. Jo, S. H. Park, B. S. Kim, H. J. Im, M. H. Lee, T. S. Min, K. T. Kim, H. G. Chae, W. P. King, J. S. Son, *Nat. Energy* **2018**, *3*, 301.

[44] W. Liu, K. C. Lukas, K. McEnaney, S. Lee, Q. Zhang, C. P. Opeil, G. Chen, Z. Ren, *Energy Environ. Sci.* **2013**, *6*, 552.

[45] J. Chen, T. Sun, D. Sim, H. Peng, H. Wang, S. Fan, H. H. Hng, J. Ma, F. Yin, C. Boey, S. Li, M. K. Samani, G. Chung, K. Chen, X. Chen, T. Wu, Q. Yan, *Chem. Mater.* **2010**, *22*, 3086.

[46] W. Zheng, P. Bi, H. Kang, W. Wei, F. Liu, J. Shi, L. Peng, Z. Wang, R. Xiong, *Appl. Phys. Lett.* **2014**, *105*, 2.

[47] G. Dong, Y. Zhu, L. Chen, *J. Mater. Chem.* **2010**, *20*, 1976.

[48] B. Chen, S. R. Das, W. Zheng, B. Zhu, B. Xu, S. Hong, C. Sun, X. Wang, Y. Wu, J. C. Claussen, *Adv. Electron. Mater.* **2017**, *3*, 1600524.

[49] G. Xing, J. Sun, Y. Li, X. Fan, W. Zheng, D. J. Singh, *Phys. Rev. Mater.* **2017**, *1*, 065405.

[50] P. Lea, *Internet of Things for Architects*, Packt Publishing, **2018**.

[51] J. Perdew, K. Burke, M. Ernzerhof, *Phys. Rev. Lett.* **1996**, *77*, 3865.

[52] K. Schwarz, P. Blaha, G. K. H. Madsen, *Comput. Phys. Commun.* **2002**, *147*, 71.

[53] G. K. H. Madsen, D. J. Singh, *Comput. Phys. Commun.* **2006**, *175*, 67.

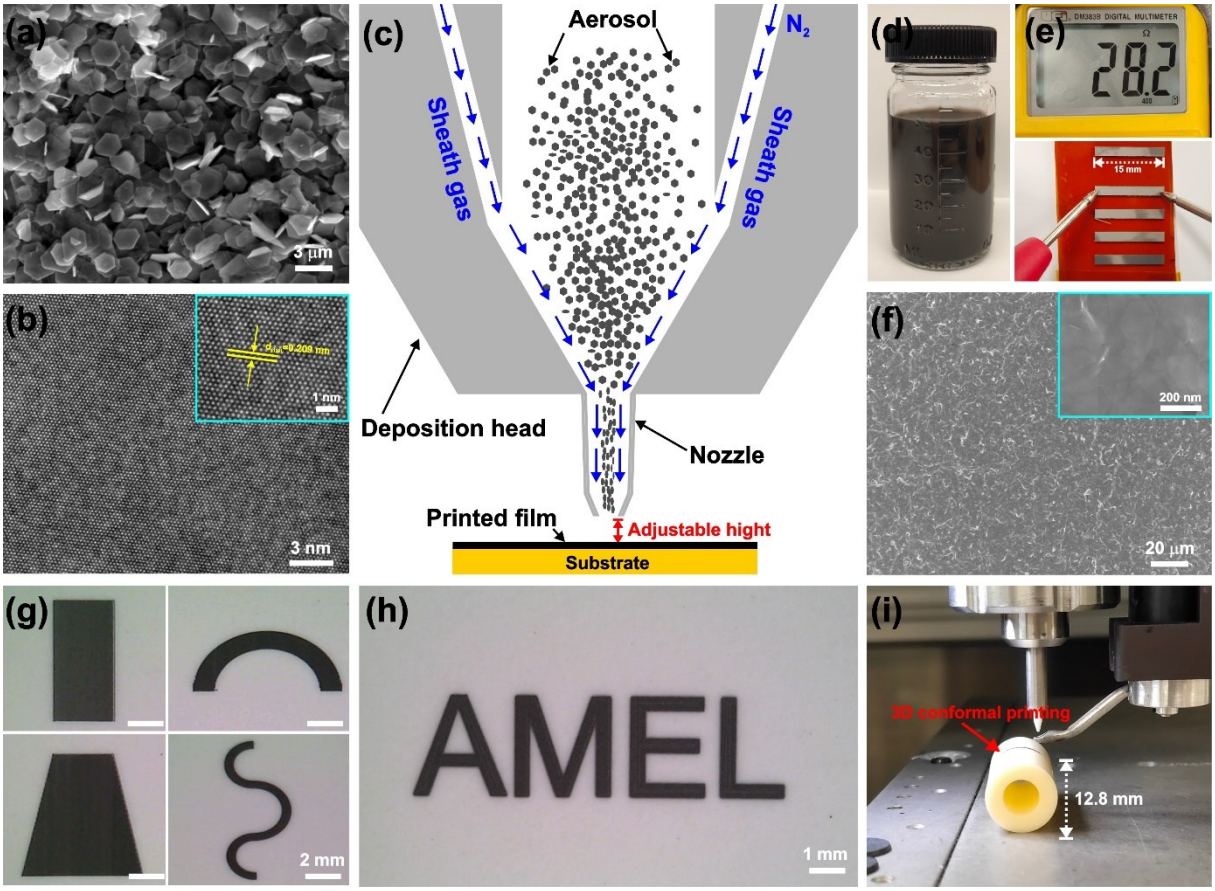

Figure 1. (a) SEM and (b) HRTEM images of Sb_2Te_3 nanoplates. (c) Schematic image of 3D conformal aerosol jet printing process using solution-processed nanostructures as building blocks. (d) Synthesized Sb_2Te_3 ink with high stability that is printable for at least three months. (e) Typical printed thin films with internal resistance around 30 Ω. (f) SEM image of Sb_2Te_3 film on polyimide after sintering at 400 ˚C for an hour. Films with designed patterns printed on various substrates: (g) printed TE legs with different shapes, (h) pattern with "AMEL" design, and (i) 3D conformal printed film on a curved surface.

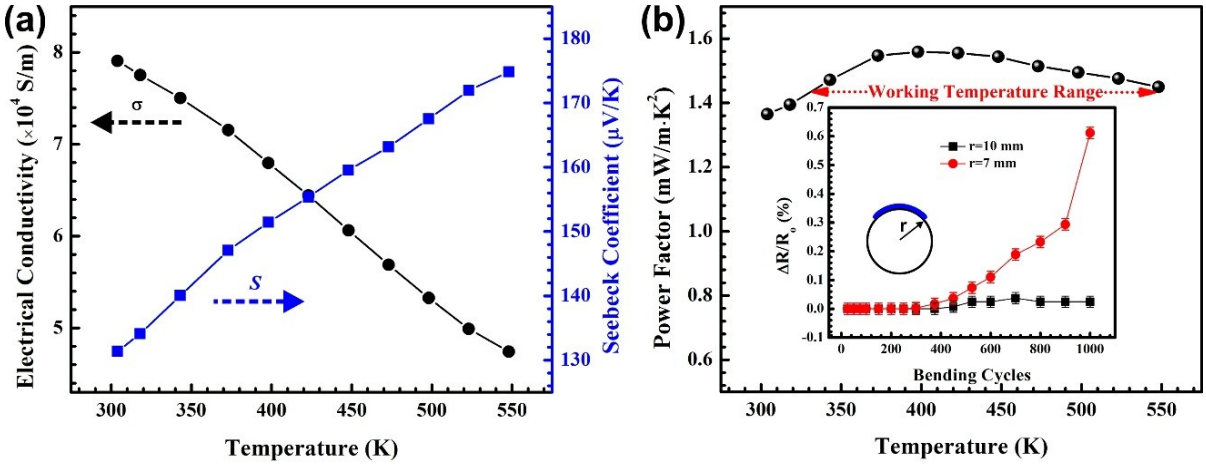

Figure 2. Temperature dependent in-plane TE properties, including (a) electrical conductivity and Seebeck coefficient, and (b) power factor of flexible Sb_2Te_3 film printed on kapton after sintering at 400 ˚C. A high power factor over a wide temperature range (350-550 K) was presented. The inset in (b) shows the excellent flexibility of the film under repeated bending tests, with R_0 the original resistance of the film and *r* the bending radius.

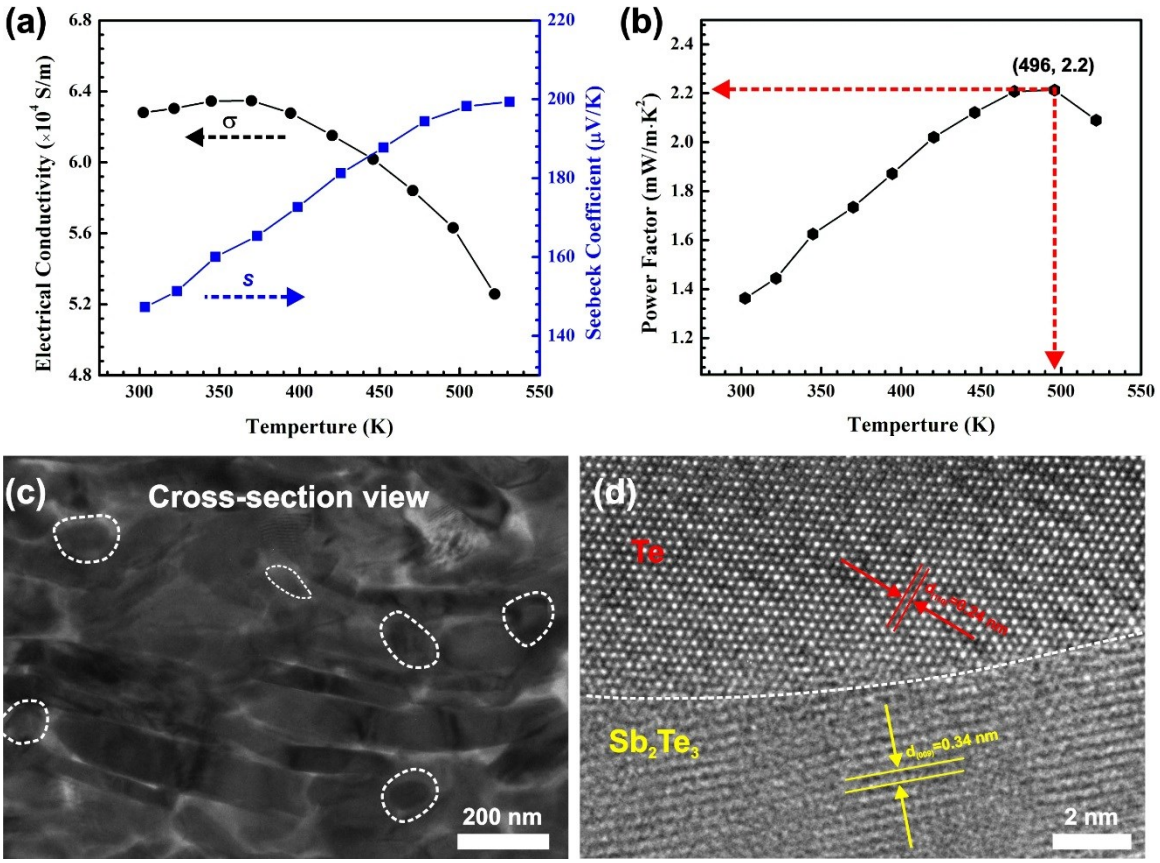

Figure 3. Temperature dependent in-plane TE properties, including (a) electrical conductivity and Seebeck coefficient, and (b) power factor of the flexible Sb_2Te_3-Te film printed on polyimide after sintering at 400 ˚C. (c) TEM and (d) HRTEM images of the interface between Te and Sb_2Te_3 from cross-plane viewpoint of the printed film. The marked dashed circles imply the existence of additional Te nanorods, with local EDS and element line-scan analysis given in SI.

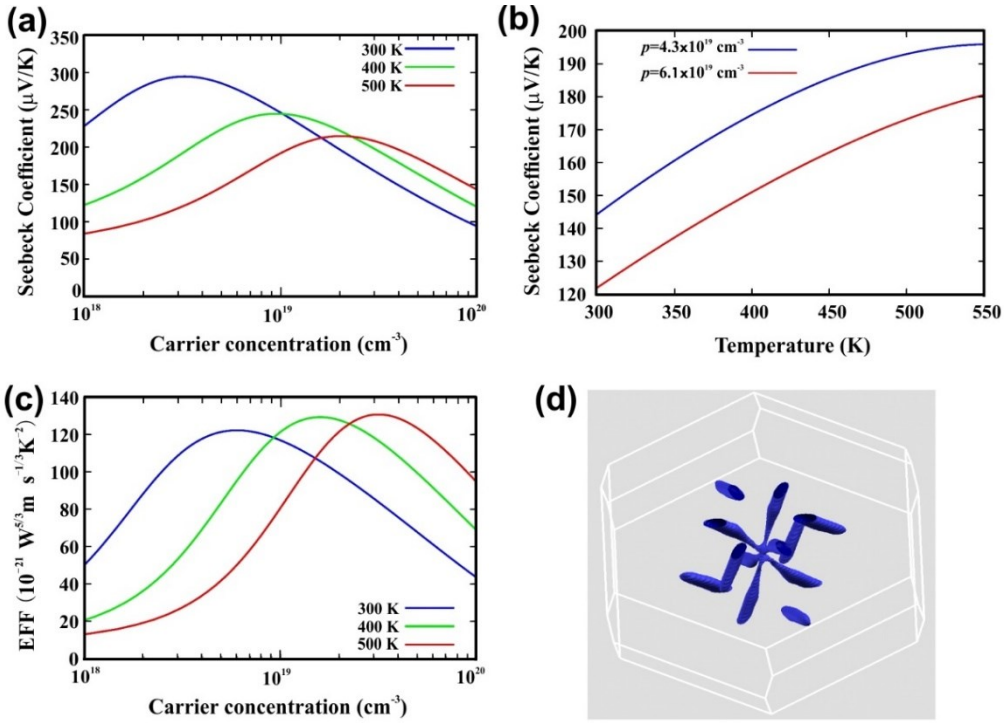

Figure 4. Transport properties from Boltzmann transport calculations and carrier pocket visualization for bulk Sb_2Te_3. (a) Seebeck coefficient as a function of carrier concentration at 300, 400 and 500 K. (b) Seebeck coefficient as a function of temperature for two fixed doping levels. (c) electronic fitness function (EFF). (d) Carrier pocket visualization showing isosurfaces 0.1 eV below the valence band maximum. Here, the transport data are direction averages.

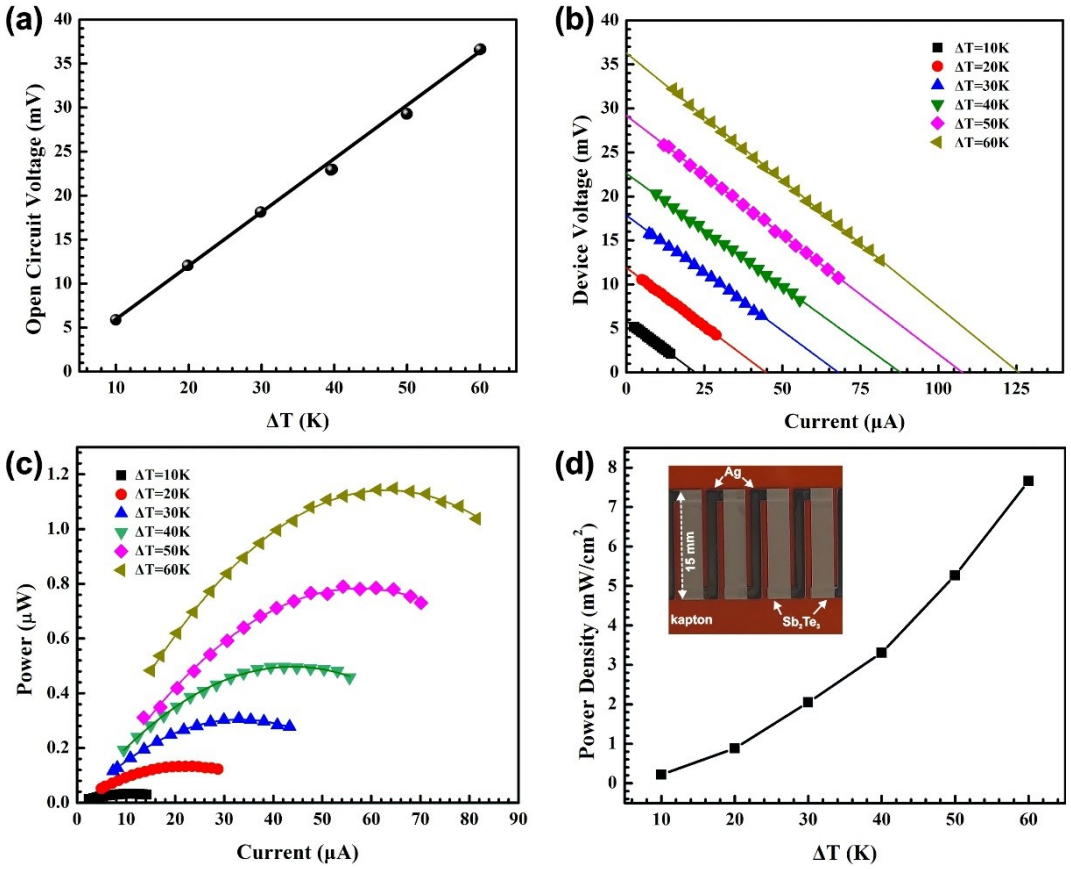

Figure 5. Performance of a flexible TE device fabricated by 3D conformal aerosol jet printing using optimized Sb_2Te_3-Te and Ag as electrodes: (a) experimental open circuit voltage (V_{oc}) vs. temperature differences (ΔT). (b) device operating voltage vs. current tested at various ΔT; (c) power output vs. electrical current at various ΔT; and (d) experimental power density tested at various ΔT (Inset: photo of the printed device).